PAPER • **OPEN ACCESS**

Synthesis of superficially modified $Ce_{1-x}(Zr + Y)_xO_{2-\delta}$ solid solutions and thermogravimetric analysis of their performance in the catalytic soot combustion

To cite this article: W N Téllez-Salazar *et al* 2021 *Mater. Res. Express* **8** 015501

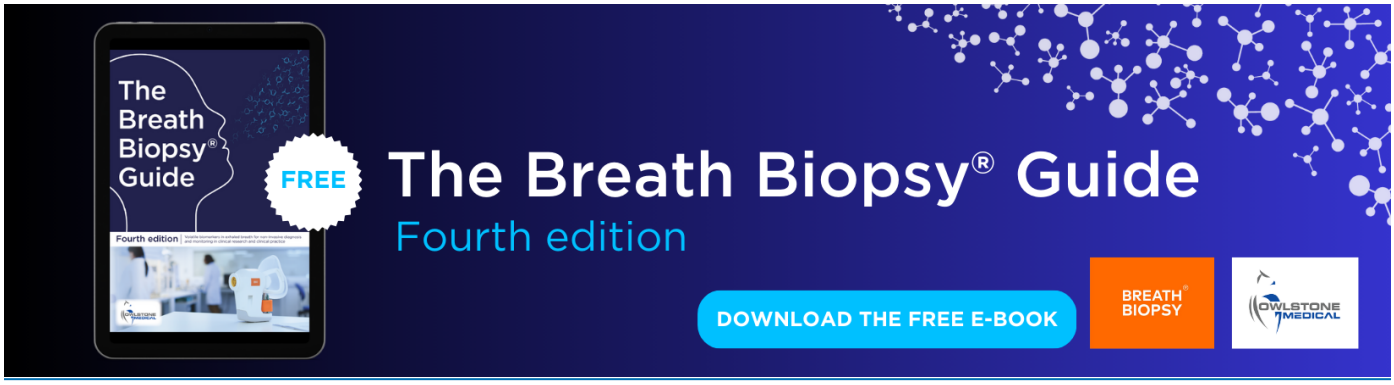

Materials Research Express

PAPER

Synthesis of superficially modified $Ce_{1-x}(Zr + Y)_xO_{2-\delta}$ solid solutions and thermogravimetric analysis of their performance in the catalytic soot combustion

W N Téllez-Salazar[1], J A Fabián-Anguiano[1], O Ovalle-Encinia[2], B H Zeifert[1], A Ezeta-Mejía[1], I C Romero-Ibarra[3] and J Ortiz-Landeros[1]

[1] Departamento de Ingeniería en Metalurgia y Materiales, Escuela Superior de Ingeniería Química e Industrias Extractivas, Instituto Politécnico Nacional, UPALM-Zacatenco, IPN Avenue, Mexico City 07738, Mexico
[2] Chemical Engineering School for Engineering of Matter, Transport and Energy, Arizona State University, Tempe, AZ 85287-6106, United States of America
[3] Unidad Profesional Interdisciplinaria en Ingeniería y Tecnologías Avanzadas, Instituto Politécnico Nacional, IPN Avenue, Mexico City 07340, Mexico

E-mail: jortizla@ipn.mx

Keywords: CeO_2, citrate-EDTA complexing method, co-doping, catalytic soot combustion, Fe_2O_3

OPEN ACCESS

RECEIVED
2 November 2020

REVISED
8 December 2020

ACCEPTED FOR PUBLICATION
23 December 2020

PUBLISHED
6 January 2021

Abstract

In this work, solid solutions of general formula $Ce_{1-x}(Zr + Y)xO_{2-\delta}$ were chemically synthesized through the so-called citrate-EDTA complexing method, wherein the doping cations Zr and Y were substituted in the ceria lattice with an equimolar amount of $0.05 \leqslant x \leqslant = 0.25$. The ternary oxides were heat-treated, and those that showed the best textural properties were superficially impregnated with Fe_2O_3 particles by the thermal decomposition method using a metalorganic precursor. The X-ray diffraction results suggest that co-doping with Zr^{4+} and Y^{3+} promotes a slight distortion of the CeO_2 cubic cell. Nevertheless, the fluorite cubic structure of the oxides remains stable after being exposed to heat treatments. Furthermore, using scanning electron microscopy and Raman techniques, the presence of deposited Fe_2O_3 and the formation of extrinsic vacancies in the materials could be corroborated. Finally, the oxides' catalytic evaluation in the soot oxidation reaction was carried out using the thermogravimetry technique. The ternary oxide with cerium molar content equal to 0.9 and impregnated with Fe_2O_3 presented excellent catalytic behavior for soot oxidation. T_{10}, T_{50}, and T_{90} temperatures were 310, 383, and 416 °C, respectively.

1. Introduction

The use of liquid fossil fuels such as diesel is of paramount importance to meet the market's large-scale demand for load, domestic, and maritime transport vehicles. Diesel-powered vehicles are notable for being highly efficient, show a low cost of operation, and long-term durability [1, 2]. However, its excessive use has given rise to the increase in soot particulate emissions that directly impact, in a negative way, the air and environmental quality [3, 4]. Soot is a carbonaceous-based matter containing other toxic substances considered highly polluting. It comes from the burning of fossil fuels and consisting of particles with sizes between 25 nanometers and 2.5 μm (PM2.5). Because these particles can easily be housed in the respiratory system, its control is imperative. According to different research and data from the World Health Organization, the housing of fine particulate matter in the respiratory system is the direct or indirect cause of more than 800 000 premature deaths per year worldwide [5–7]. Therefore, strict measures have been taken into account to control and mitigate particulate soot emissions produced mainly by automotive vehicles. Some of them include improving engine design through fuel treatment, modifications to fuel formulation, and the use of additives. However, these actions have underperformed in soot emissions reduction [8]. In this sense, filters have been developed for diesel particle control (DPF), which is a technology based on the manufacture of metal foams or honeycomb-structured ceramics with symmetrical or asymmetrical channels to physically capture soot particles and prevent

their indiscriminate emission into the atmosphere [9–11]. As the exhaust gas flows through the porous walls inside the filters, the soot is trapped. However, capture becomes inefficient as soot clogs the filter channels and causes back pressure in the DPF, directly affecting the engine performance [12, 13]. Some regeneration methods, so-called active, passive, and mixed (active-passive) methods, have been studied to enhance the filter's performance and counteract the effect of backpressure. Each of these methods requires high temperatures (~600 °C) and the presence of a certain amount of oxidant species (O_2 and NO_x) in the system [14]. Therefore, to reduce the high temperatures required for the regeneration process, several catalytic materials have been coupled to the DPF system to facilitate the combustion of soot at a lower temperature; such is the case of Pt and Pd-based catalysts [15, 16]. However, these catalysts are expensive and exhibit poor catalytic performance in environments where heavy hydrocarbons are involved [16]. Therefore, in the search for better catalysts exhibiting excellent performance in soot oxidation at low temperatures, ceramic oxides have been studied, such as metal oxides with ionic conduction properties [17–19]. Due to the mobility properties of oxygen ions in its crystalline network and the high concentration of oxygen species that can be achieved on the surface of the material, they have been studied for the post-combustion elimination of NO_x and soot coming from diesel engines. The results have shown that using ionic and electro-ionic conductor oxides such as the fluorites and perovskites, removing soot can be ensured at low temperatures (350 –400 °C), obtaining mainly CO_2 gas as a combustion product. However, there are still significant challenges in applying such catalysts, such as reaction kinetics and the operating temperature. Some of the most important advances have been found in the study of ceria-based catalysts. CeO_2 is known to be an oxidizer due to its ability to store oxygen. Therefore, cerium oxide-based catalysts have been further developed by adding metals and metal oxides, such as Ag, Co_3O_4, Fe_2O_3, and MnO_x, to name a few, which have been evaluated in the soot oxidation reaction [20–25]. For example, considerable improvements have been reached on the development of efficient Fe_2O_3 containing catalysts to promote the soot oxidation at low temperatures wherein the Fe_2O_3 phase acts as a supported or unsupported active phase [24–26]. Like other oxides exhibiting oxi-reduction properties, the reaction mechanism on bulk Fe_2O_3 involves superficially oxygen defect sites resulting from the oxygen transfer from the catalyst to the soot during the oxidation reaction. These defect sites in the catalyst are refilled either by bulk diffusion of oxygen species or re-oxidation promoted by the oxygen-containing gas phase. Moreover, the bulk's oxygen deficiency is balanced by the migration of oxygen species coming from the sub-surface [27]. Iron-containing catalysts of the Fe_2O_3–CeO_2 system have shown excellent properties. Depending on the synthesis method, it has been obtained the incorporation of Fe^{3+} into CeO_2 bulk or superficially dispersed Fe_2O_3 clusters on bulk CeO_2-based materials [24, 25].

As described, results have shown that ceria-based catalysts exhibit good catalytic behavior. However, because its storage and oxygen release capacity depends heavily on the redox reaction between Ce^{3+} and Ce^{4+}, it has been suggested to study the doping and co-doping of the pure oxide to promote a higher concentration of extrinsic oxygen vacancies in the crystal lattice, and this way to enhance the oxygen exchange process which is related with the kinetics of the soot combustion reaction [28, 29]. This work studied the CeO_2 co-doping by introducing Zr^{4+} and Y^{3+} into the ceria lattice to develop ternary oxides of the general formula $Ce_{1-x}(Zr + Y)_xO_{2-\delta}$ with different x-values. As mentioned, the idea is to promote the formation of defects (oxygen vacancies) involved in the oxygen ion conduction property. The catalytic properties of oxides were studied by thermogravimetry (TGA), evaluating several samples prepared by mixing the different catalysts and black carbon that serves as a soot model. Hence, Fe_2O_3 nanoparticles were superficially loaded in the selected ternary oxides to re-evaluate their catalytic performance in the soot oxidation, in a temperature range of between 30 –700 °C.

2. Materials and methods

2.1. Synthesis and characterization of the catalyst

The citrate-EDTA complexing method was used to chemically synthesize the ternary oxides with the general formula $Ce_{1-x}(Zr + Y)_xO_2$ [30, 31]. Aqueous solution precursors were prepared under constant agitation and 70 °C by using the stoichiometric amounts of the $Ce(NO_3)_3 \cdot 6H_2O$ (99% Sigma-Aldrich), $ZrOCl_2 \cdot 8H_2O$ (98% Sigma-Aldrich), and $Y(NO_3)3 \cdot 6H_2O$ (99% Sigma-Aldrich). The complexing agents were added in a molar ratio of CA (anhydrous citric acid): total metal cations of 2:1, and EDTA: dopant cations (Y + Zr) of 1:1. The final pH of the system was adjusted to 5 by adding diluted HNO_3. Experimental conditions were set to ensure the formation of the citrate and EDTA (ethylene-diamine-tetra-acetic acid) complexes based on the distribution diagrams of metal ions containing species constructed using the Hydra-Medusa software [30]. Then, the temperature was raised to 90 °C to evaporate the water and obtain a gel-like precursor. At this point, the system's agitation was removed, and the temperature was increased to 300 °C to promote the self-combustion process to eliminate the organic components mostly. The obtained powders were heat-treated in an air atmosphere at 600 °C and 900 °C for 10 h. In a second stage, selected oxides of different composition were

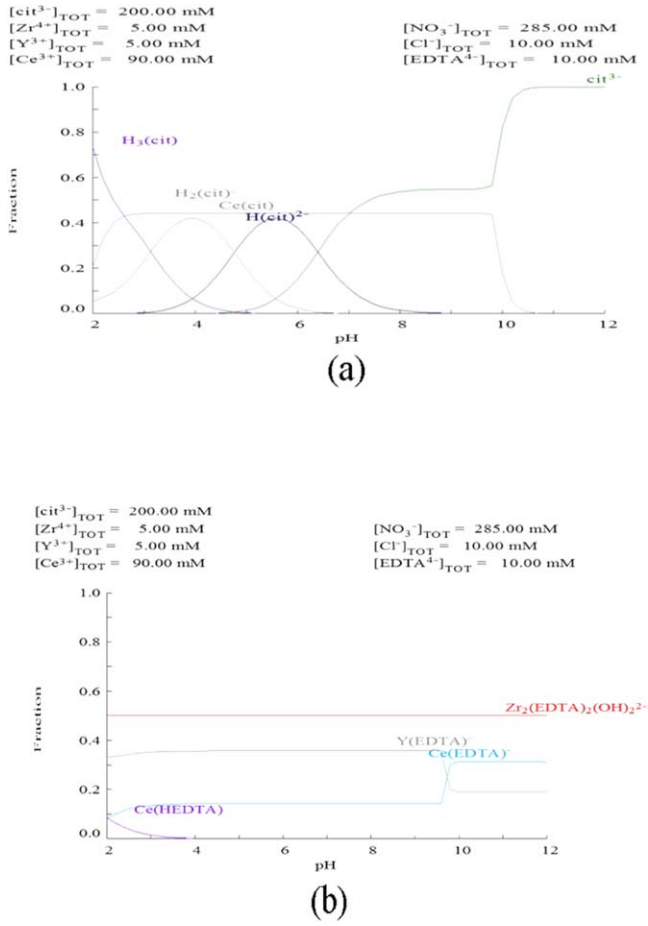

Figure 1. Distribution diagrams of metal ions containing species as a pH function: (a) citrate containing and (b) EDTA containing complexes.

loaded with Fe_2O_3 particles, following a modified procedure based on the use of metalorganic precursors [32]. The process is about the thermal decomposition of iron acetylacetonate $Fe(C_5H_7O_2)_3$ and was carried out in two stages; first, under vacuum to promote the precursor's decomposition and subsequently, under dry air flow to ensure the formation of the Fe_2O_3 phase. Stoichiometric amounts of $Fe(C_5H_7O_2)_3$ were used to obtain a final deposit Fe_2O_3 of 8 wt% based on the cerium oxide that acts as support. The structural analysis of the obtained materials was performed by X-ray diffraction using a BRUKER D8 Focus diffractometer equipped with a Cu-Kα radiation source. The equipment was operated at 35 kV and 25 mA. The analyses were done in a 2θ range of 20–80° with increments of 0.02 degrees. The crystalline phases were identified with the JCPDS database, and the crystalline structure was refined by the Rietveld method using the BGMN program and the Profex graphical interface [33]. The Lorentzian function was used to model the peak profiles, and the Debye-Scherrer equation was used to determine the anisotropic crystal size [34]. The textural properties of the oxides were determined by the N_2 physisorption technique by using an Autosorb-iQ equipment from Quanthachrome, USA. Prior to analysis, the samples were heat-treated at 150 °C for 4 h under vacuum. Surface area, pore volume, and average pore diameter values were determined using the BET and BJH models. The microstructural and morphological features of the oxides were investigated by scanning electron microscopy by using a JSM6701F microscope from JEOL. The presence and distribution of constituents in the iron-containing oxides were corroborated by SEM-EDS analysis by carrying out the elementary mappings technique. Raman spectroscopy analysis was conducted by using a Raman DRX2 Thermo- Olympus Scientific Microscope. For each measurement, a laser of 523 nm wavelength, a controlled intensity between 0.1–10 mW, and an objective lens of 20 X/0.4 BD with a spot size of 2.1 μm and a slit aperture of 25 μm.

2.2. Catalytic evaluation

To determine the catalytic activity and oxidation temperature of soot, selected materials (those exhibiting the best textural properties) were evaluated by thermogravimetry. The analyses were performed on the mixtures prepared mechanically with the different catalysts and Printex-U, which is a commercial pigment based on carbon black. This carbonaceous compound has been extensively used as a model of soot particles.

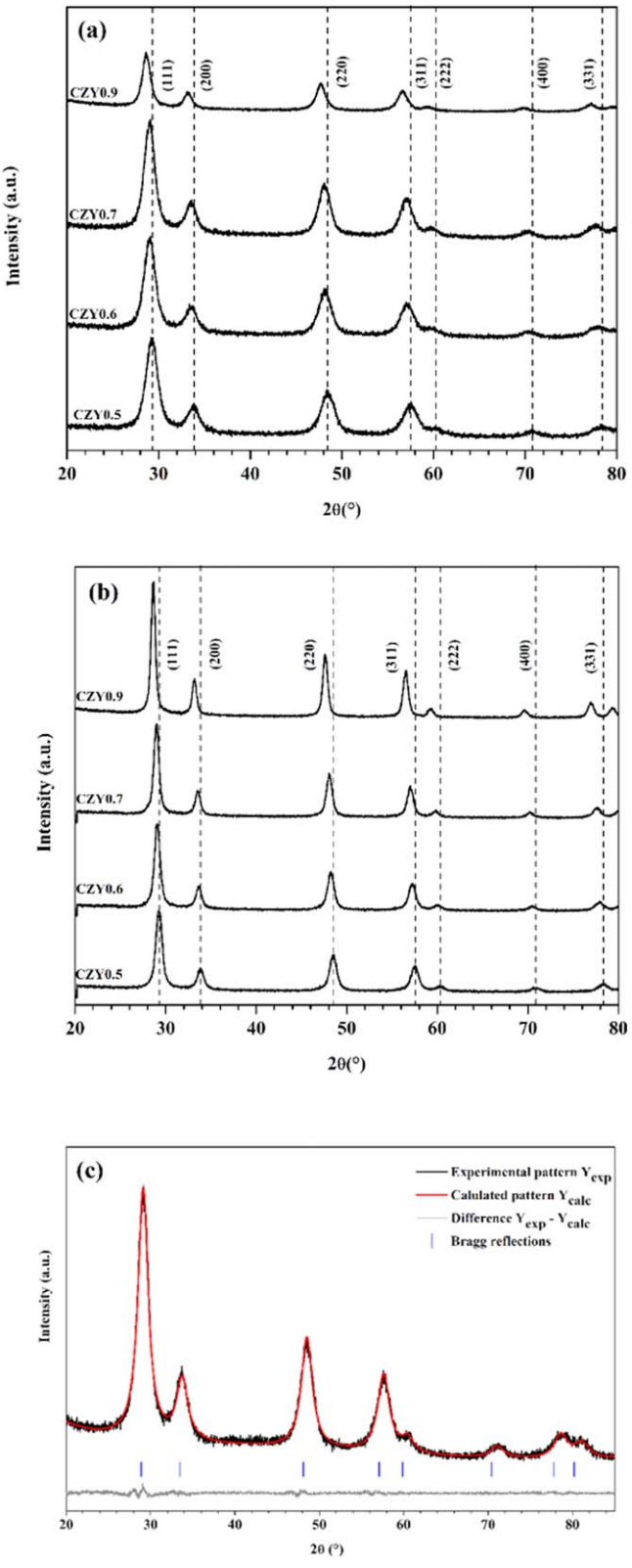

Figure 2. X-ray diffraction patterns of ternary oxides obtained by the citrate-precursor chemical route: (a) thermal treatment at 600 °C for 10 h, (b) thermal treatment at 900 °C for 10 h, and (c) example of XRD data processing by Rietveld method.

Measurements were made on a thermobalance model STA Regulus 2500 from Netzch. TGA experiments were performed under an air atmosphere and a temperature range between 30 –700 °C. For the obtained results to be comparative, a weight ratio of catalyst to Printex-U was established as ~9:1; this specific proportion was set based on several previous reports [24, 26]. Moreover, the large amount of catalyst used relative to carbon guarantees a high number of contact points in the sample during TGA analysis. The sample mixtures were prepared by hand, mixing the constituents very gently in a mortar to get a loose contact mode.

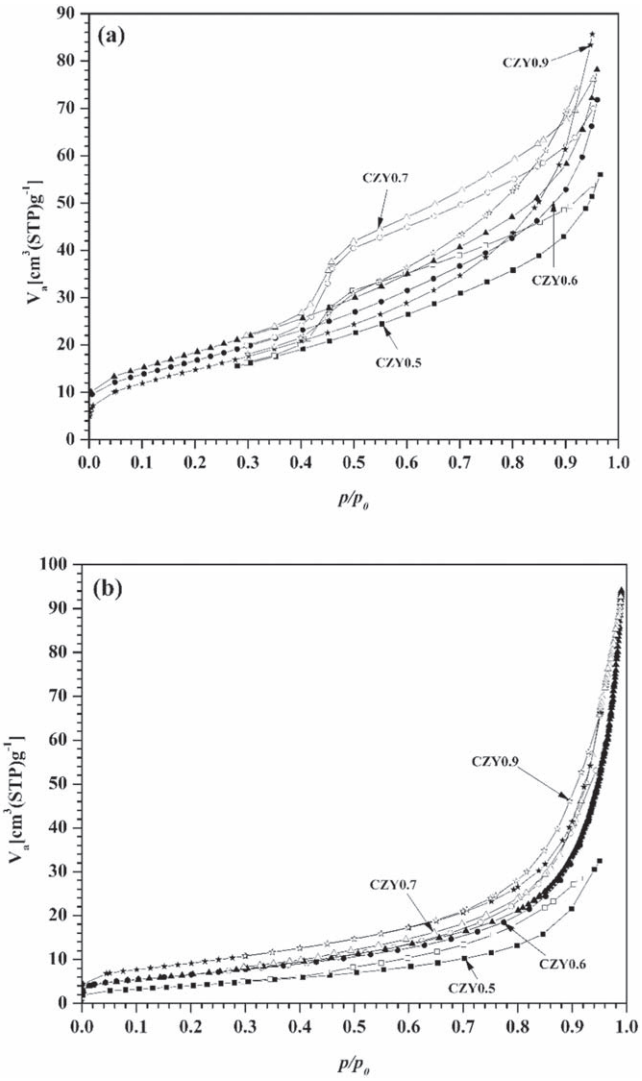

Figure 3. N_2 adsorption-desorption isotherms of different ternary oxides: (a) thermal treatment at 600 °C for 10 h and (b) thermal treatment at 900 °C for 10 h.

3. Results and discussion

3.1. Experimental conditions for the materials synthesis

The citrate-EDTA complexing method was chosen to guarantee the solid solution formation starting from a homogeneous aqueous phase. The chelating agents modify the aqueous hydrolysis chemistry of the involved metal cations (Ce^{3+}, Y^{3+}, and Zr^{4+}) to form metal complexes and resulting in a gel precursor, which is very homogeneous in composition. The complexes formation (in terms of pH and chelating agents' concentration) was analyzed through the constructed chemical equilibrium diagrams. Figure 1 shows the chemical species in the studied system, considering pH values ranging from 2 to 12. The concentrations of the Ce^{3+}, Y^{3+}, Zr^{4+}, citrate (cit^{3-}), and $EDTA^{4-}$ are 90, 5, 5, 200, and 10 mM, respectively, that agrees with the correspondent molar ratio of chelating agents and metal cations experimentally studied. Figure 1(a) shows the obtaining of citrate containing species. In the wide range of pH values from 3–10, cerium citrate complex is formed; moreover, other species were observed; for example, at pH 5, the different species are [Ce(Cit)], $[H(Cit)^{2-}]$ and $[H_2(Cit)^{2-}]$. On the other hand, figure 1(b) shows the distribution of EDTA containing species. In this case, the formed complexes include the three different metal cations in the system. Different from cerium, the dopant containing complexes are mainly formed with the EDTA but not with citric acid. At pH 5, the observed different species include $[Zr_2(EDTA)_2(OH)_2^{2-}]$, $[Y(EDTA)^-]$, and $[Ce(EDTA)^-]$. In this case, as previously reported, the use of alternative complexing agents, along with citric acid, can promote the formation of more stable metal-chelate species [30]. Here, EDTA is particularly important as Zr cations are less prone to form complexes with the citric acid. Besides, pH was established as 5 for the materials synthesis as zirconium cations could be hydroxylated as $Zr(OH)_5^-$ or even form $ZrO_{2(s)}$ at alkaline conditions.

Table 1. Crystallographic data of cerium-based ternary oxides depending on composition and heat treatment, obtained through Rietveld refinement measurements.

$Ce_{1-x}(Zr + Y)_xO_{2-\delta}$ (1−x values) 600 °C	Crystal size (nm) (100)	(111)	Lattice parameter ***a*** (nm)	Rwp	χ^2
0.5	5.0	5.4	0.534	5.75	1.175
0.6	5.2	5.7	0.536	1.46	0.591
0.7	5.8	6.1	0.537	0.87	0.460
0.9	7.1	7.8	0.539	0.19	0.142
1.0	21.4	22.7	0.541	5.48	1.453
900 °C					
0.5	9.4	10.7	0.533	5.84	1.147
0.6	10.3	11.7	0.536	1.04	0.559
0.7	12.0	13.1	0.537	0.56	0.414
0.9	15.5	16.1	0.540	0.26	0.268
1.0	86.0	97.0	0.541	0.55	0.436

Table 2. Textural properties of the thermal-treated ternary oxides at 600 and 900 °C.

Ternary System	Temperature (°C)	V_m (cm^3(STP)/g)	S_{BET}(m^2 g^{-1})	Total pore volume ($p/p_0 = 0.954$) (cm^3 g^{-1})	Average pore diameter (nm)
CZY0.5	600	11.891	**51.75**	0.086	6.701
	900	3.707	**16.13**	0.050	12.453
CZY0.6	600	14.422	**62.77**	0.111	7.078
	900	5.558	**24.19**	0.091	15.145
CZY0.7	600	15.958	**69.45**	0.120	6.958
	900	5.875	**25.56**	0.145	22.708
CZY0.9	600	12.861	**55.98**	0.1324	9.460
	900	7.747	**33.72**	0.1021	12.112

V_m: N_2 adsorbed volume.
S_{BET}: specific surface area.

3.2. Structural and microstructural characterization of catalyst

Figure 2 shows the x-ray diffraction patterns of the different heat-treated oxides at 600 °C and 900 °C. As shown in figures 2(a) and (b), the diffraction patterns of the different samples show the characteristic peaks of (111), (200), (220), and (311) planes, all of them belonging to a fluorite-type cubic structure of *fm3m* space group corresponding to the JCPDS card number 034-0394 (Joint Committee on Powder Diffraction Standards). Qualitatively speaking, it was observed that the heat treatment at 900 °C increases the crystallinity degree of the oxides. Rietveld refinement was performed to investigate the effect of doping agents on the crystalline structure of CeO_2. Table 1 shows the obtained crystallographic data. As the amount of Zr^{4+} and Y^{3+} dopants in the oxide increases, the lattice parameter decreases. In addition, the increase in temperature in the heat treatment of oxides, along with the increase in the amount of doping agents, promotes a decrease in the mean crystal size representing the planes (100) and (111). This effect was more noticeable for powders treated at 900 °C than samples treated at 600 °C. These results demonstrate that cerium oxide doping with Zr^{+4} and Y^{+3} in equimolar amounts of 0.05, 0.15, 0.20, and 0.25 promotes slight changes in the dimensions of the CeO_2 cell related to its distortion, decreasing of crystallite size, and displacement of diffraction peaks at larger angles, due to the difference between the ionic radii of the Ce^{+4}, Zr^{4+} and Y^{+3} (0.97, 0.84, and 1.019 Å respectively) [35]. The average crystallite size increases by the effect of the heat treatment temperature in all cases. Besides, the results suggest the high stability of the CeO_2 cell at high temperatures, as the transformation from the cubic to the tetragonal phase was not observed.

Figure 3 shows the N_2 absorption-desorption isotherms of the different samples. According to the IUPAC's conventional classification, the isotherms in figures 3(a) and (b) correspond to type IV isotherms. However, by showing hysteresis loop type H_3, but not a clear plateau at high *P/Po* values, some authors have called these isotherms type II-b, which are assigned to materials consisting of soft agglomerates of fine particles forming interparticle mesopores [36]. On the other hand, in figure 3(b), it is observed that the heat treatment of powders at 900 °C caused, in some cases, isotherms type II related to the behaviour of a non-porous solid or with a lower volume of pores [37]. There was not observed a clear trend for the specific surface area values to change with the composition. The highest surface area values were for samples exposed to 600 °C; this series of samples presented specific area values (S_{BET}) ranging from 51.7–65.3 $m^2 \cdot g^{-1}$. Therefore, from the results obtained by

Table 3. Composition of the different impregnated materials. The % weight of the Active Phase (Fe_2O_3) was obtained by the EDS technique.

Element	wt%	at%	Fe_2O_3 wt%
	CZY0.7Fe		
O	19.22	64.59	**5.2**
Fe	3.62	3.49	
Zr	3.65	2.21	
Y	7.36	4.33	
Ce	66.15	25.38	
	CZY0.9Fe		
O	22.88	70.01	**6.2**
Fe	4.31	3.78	
Zr	2.79	0.71	
Y	1.3	1.51	
Ce	66.72	24.00	

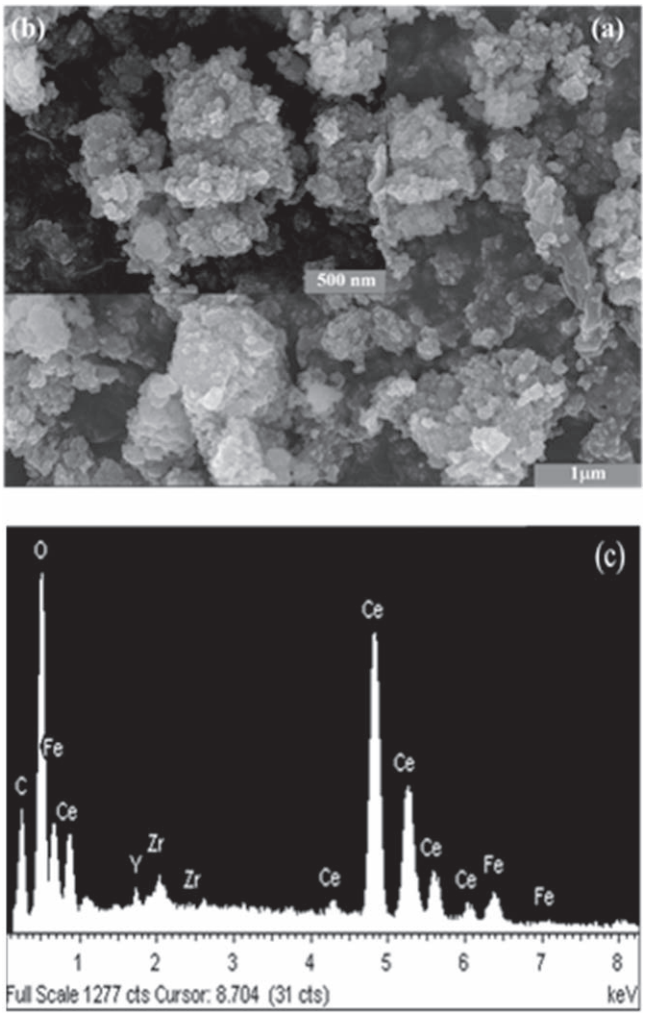

Figure 4. MEB analysis: (a) and (b) secondary electrons images of CZY0.9Fe oxide, and (c) general microanalysis by MEB-EDS technique.

N_2 physisorption, the samples thermally treated at 600 °C have the best textural properties. Based on the above, selected samples of this series were impregnated with Fe_2O_3 nanoparticles for further catalytic evaluation in soot combustion. Table 2 shows the specific surface area, pore volume, and the average pore size values resulting in the different ternary oxides by their calcination at 600 and 900 °C.

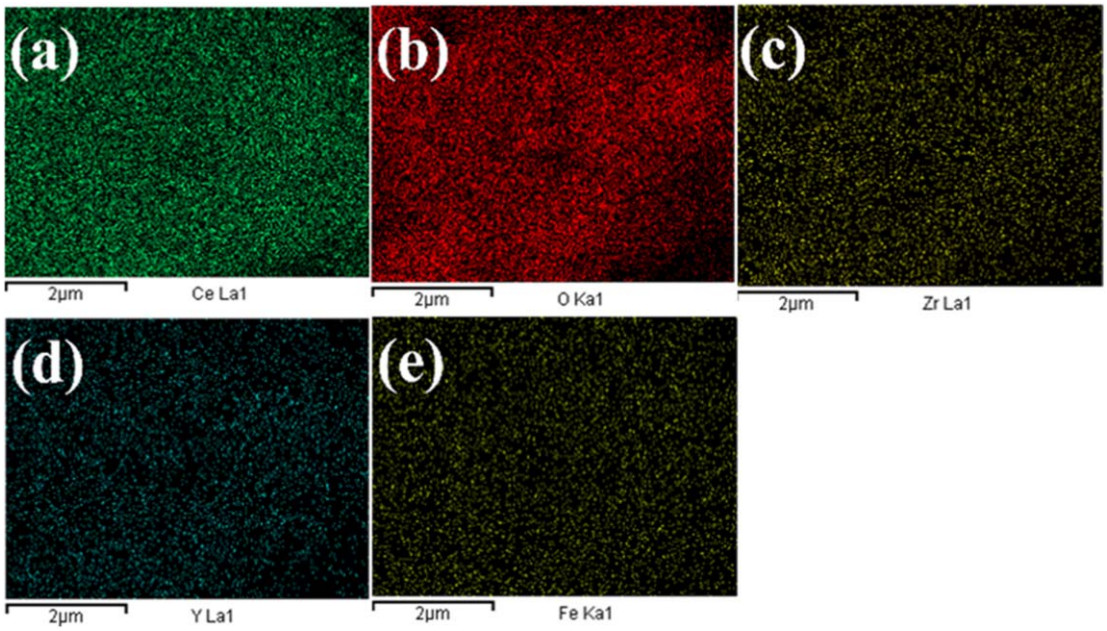

Figure 5. Elemental mapping and distribution of the different elements in the CZY0.9Fe oxide.

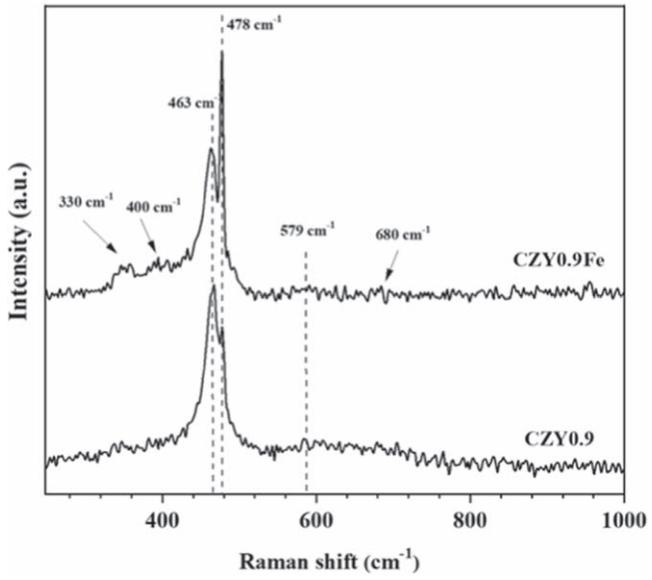

Figure 6. Raman spectra of the CZY0.9 and CZY0.9Fe samples; it is shown the wavelength range from 300 to 1000 cm^{-1}.

Generally speaking, the function of the CeO_2-based catalysts for soot combustion is to catch the oxygen from the gas phase and transfer it, as active oxygen species, to the soot particle surface. From this point of view, the catalyst performance is directly linked to their specific surface areas and surface properties because it is in the catalyst surface wherein the formation and exchange of oxygen species occur [24, 25]. Therefore, considering their obtaining textural properties, CZY0.7 and CZY0.9 samples subjected to a heat treatment of 600 °C were chosen to be further superficially modified through their impregnation with Fe_2O_3 to fabricate the final catalyst. The selected samples exhibited the highest total pore volume values and high specific surface areas. Table 3 shows the results obtained from the Fe_2O_3 content of the aforementioned oxides, which now on will be identified as CZY0.7Fe and CZY0.9Fe.

Figure 4 shows the results obtained from the MEB analysis of CZY0.9Fe oxide. This sample was the one that presented a Fe_2O_3 content closer to the theoretical value (8%wt). As shown in figures 4(a) and (b), the oxide is made up of irregularly shaped porous agglomerates with sizes of around 0.1–2 μm. These features are commonly observed in powder materials produced by the combustion synthesis process following by heat treatment.

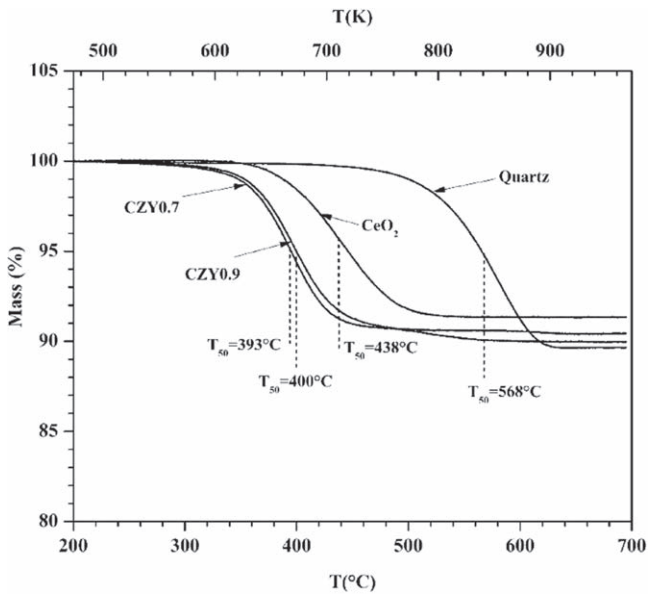

Figure 7. Catalytic soot oxidation evaluation by TGA and using CeO_2, quartz, and the ternary oxides CZY0.7 and CZY0.9 as catalysts.

It is important to mention that through the secondary electron technique, the Fe_2O_3 nanoparticles that were deposited by the thermal decomposition route were not directly observed. However, the general MEB-EDS micro-analysis in figure 4(c) confirms the presence of iron belonging to these particles, as well as the doping elements in cerium oxide. Figure 5 shows through an elementary mapping, the distribution of the different elements in the CZY0.9Fe ternary oxide. It is observed that the signals of Ce and O (figures 5(a) and (b)) are in agreement with the EDS spectrum in figure 5(c); these signals are found with greater intensity because they are the main elements that constitute the ternary oxide. Figures 5(c)–(e) show the presence of the Zr and Y doping agents and the Fe corresponding to the deposit made on the material. Therefore, it should be noted that the manufacture of ternary oxides modified with a deposit of highly dispersed nanoparticles is successfully obtained by combining the synthesis methods by precursor citrate, followed by the process of thermal decomposition impregnation.

The ceria-based solid solutions were analyzed by Raman spectroscopy. Figure 6 shows the pristine and surface modified oxides' spectra in a wavelength range of 300–1000 cm^{-1}. In both cases, the peak at 463 cm^{-1} is directly related to the symmetrical F2g vibrational mode of the oxygen atoms surrounding the Ce^{4+} cation in the fluorite oxide of the ceria [38]. Because the vibrational mode of the Ce^{4+} depends on the movement of the lattice oxygen, the characteristics of the peak, such as width and position, are highly sensitive. The vibrational mode in 579 cm^{-1} is attributed to the formation of oxygen vacancies D1 as a result of the charge compensation effect of doping cations [39]. In this sense, the formation of extrinsic vacancies in the material can be explained through the chemistry of defects in Ec (1).

$$ZrO_2 + Y_2O_3 \overset{CeO_2}{\rightarrow} Ce_{Ce}^{x} + Zr_{Ce}^{x} + 2\,Y_{Ce}^{\prime} + V_{\ddot{O}} + O_O^x \quad (1)$$

According to the Kröger-Vink, notation O_O^x and $V_O^{\cdot\cdot}$ represent the oxygen of the network and the oxygen vacancies, respectively. On the other hand, and different from the pristine sample, the Raman spectra of the superficially modified sample shows two weak peak signals in the wavelength range of 300–400 cm^{-1} that were attributed to Eg modes of the Fe_2O_3 [40]. The small peak at 680 cm^{-1} has also been reported for the Fe_2O_3 oxide, proving its successful deposition on the ternary oxide surface; sample (CZY0.9Fe) [41].

Moreover, the peak signal that appears at 478 cm^{-1} can be attributed to the presence of surface oxygen vacancies [42]. It is noticeable that the impregnated sample shows a higher peak intensity than the pristine ternary oxide. Qualitatively speaking, this result suggests the enrichment of iron cations on the catalyst surface. Actually, the Fe–O–Ce species in the Fe_2O_3–CeO_2 interface have been identified as active sites for the soot oxidation reaction [24, 25]. The aforementioned feature in the catalyst surface can be described by the migration of Fe^{3+} ions into the support lattice at a superficial level (equation (2)).

$$Fe_2O_3 \overset{CeO_2}{\rightarrow} Ce_{Ce}^{x} + 2Fe_{Ce}^{\prime} + V_{\ddot{O}} + O_O^x \quad (2)$$

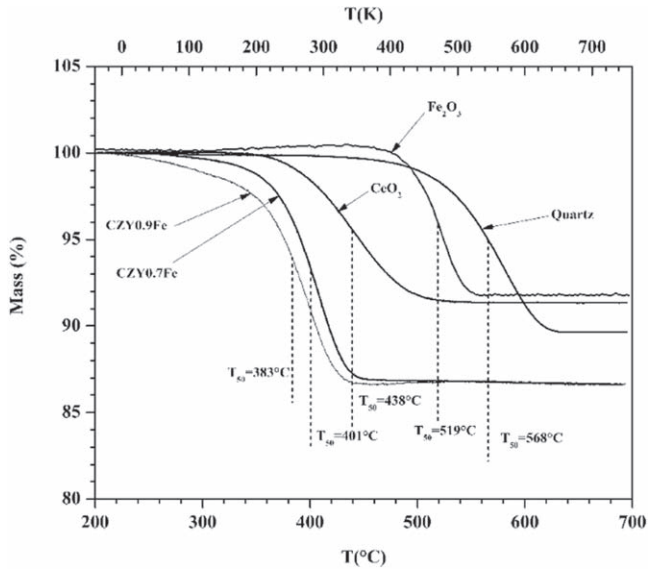

Figure 8. TGA curves of the soot oxidation tests for quartz, Fe_2O_3, CeO_2, and the CZY0.7Fe and CZY0.9Fe ternary oxides catalysts.

Table 4. T_{10}, T_{50}, and T_{90} calculated values from thermogravimetric curves analysis performed to different catalysts with and without impregnation.

Catalyst	T_{10}	T_{50} (°C)	T_{90}
Quartz	501	568	606
Fe_2O_3	494	519	540
CeO_2	385	438	487
CZY0.7	347	393	433
CZY0.9	353	400	465
CZY0.7Fe	353	401	431
CZY0.9Fe	310	383	416

3.3. Catalytic evaluation

Figure 7 shows the results of the catalytic evaluation of CZY0.7 and CZY0.9 samples. Besides, the results obtained for pure CeO_2 and quartz are shown. In the latter two cases, the materials were used as a baseline and for comparative purposes. In fact, in the case of quartz, which is an inert material, it was used to describe the uncatalyzed thermal decomposition process of the Printex-U. The thermogravimetric curves show the analysis carried out in a temperature range between 200 °C–700 °C, which considers only the soot combustion process's weight losses. It is observed that the average combustion temperature (T_{50}) is very similar for the ternary ceria-based oxides; actually, both improve significantly, the oxidation reaction of soot compared to the undoped ceria since they decrease the average combustion temperature to values of 393 and 400 °C for CZY0.7 and CZY0.9 samples respectively.

Figure 8 shows soot oxidation analyses using ternary oxides impregnated with Fe_2O_3, corresponding to CZY0.7Fe and CZY0.9Fe samples. It is also shown the result obtained for pure Fe_2O_3 commercial powders, which is included as baseline data. Comparing the different thermogravimetric curves, the thermal decomposition process conducted without catalyst (using quartz) starts at approximately 500 °C, exhibiting total weight loss when it reaches 620 °C. On the other hand, in the case of CeO_2, the decrease in the soot combustion temperature was observed, which is promoted by the redox nature of the cerium oxide. Values representing 10, 50, and 90% of conversion were carried out at temperatures of 385 °C, 438 °C, and 487 °C, respectively. These results are consistent with the reported values for CeO_2 catalysts that have been synthesized with different types of morphology [43]. Contrary to the moderate activity exhibited by the pure Fe_2O_3 coarse powders, both impregnated ternary oxides, CZY0.7Fe and CZY0.9Fe, strongly promote the soot oxidation process. The values to carry out the soot conversion at T_{10}, T_{50}, and T_{90} were 353 °C, 401 °C, and 431 °C for CZY0.7Fe oxide. For CZY0.9Fe oxide, the T_{10}, T_{50}, and T_{90} temperatures were 310 °C, 383 °C, and 416 °C, respectively. The results support the obtaining of extrinsic oxygen vacancies in the material due to co-doping, as well as jointly facilitating the intrinsic redox properties of the base material ($Ce^{4+} \leftrightarrow Ce^{3+}$). The deposited

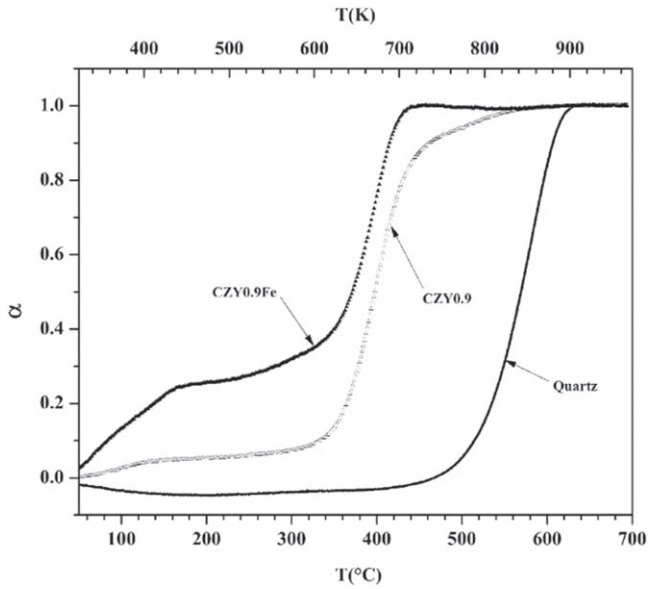

Figure 9. Reaction extent according to the combustion reaction temperature for CZY0.9, CZY0.9Fe, and quartz oxides.

Fe_2O_3 significantly improves the soot combustion reaction. Based on the Raman analysis, this fact is explained as the addition of Fe_2O_3 is able to increase the oxygen vacancies concentration, especially on the ceria surface. Hence, the superficially modified catalyst activity must also rely upon the oxi-reduction properties of the deposited small fine Fe_2O_3 particles. Overall, this study demonstrates that the proposed oxides have potential applications as catalysts in soot combustion and possibly in other oxidation reactions such as the oxidation of CO and VOCs.

Table 4 shows the T_{10}, T_{50}, and T_{90} values of the different oxides evaluated. It is observed that the Fe_2O_3 deposit causes a decrease in the combustion temperature of soot in ternary oxide with a molar cerium composition of 0.9. The T_{50} value for this material is 383 °C. The remarkable enhancement on the catalytic activity of CZY0.9Fe sample in comparison to the CZY0.7Fe and their respective supports could be attributed to the higher amount of Fe_2O_3 obtained (6.2%wt). Therefore, further studies must be focused on optimizing the amount of the Fe_2O_3 as this phase clearly acts as a promoter of the soot oxidation reaction.

3.4. Kinetic study of the soot oxidation reaction

Based on the catalytic performance presented by CZY0.9Fe oxide, the kinetic reaction study was performed to determine the apparent activation energy *Ea* and pre-exponential factor A by means of the Coats-Redfern method considering equation (3):

$$\log \frac{g(\alpha)}{T^2} = \log\left[\frac{AR}{\beta E_a}\left(1 - \frac{2RT}{E_a}\right)\right] - \left[\frac{E_a}{2.303RT}\right] \tag{3}$$

In this equation, β is the heating ramp under which the reaction occurs (C min^{-1}), T is the temperature in Kelvin, and R is the universal gas constant [44]. In this model, the $g(\alpha)$ function describes the phenomena that take place during the soot oxidation reaction. This function is considered that corresponds to a spherical shrinkage model, which is represented by equation (4) [45].

$$g(\alpha) = 1 - (1 - \alpha)^{\frac{1}{3}} \tag{4}$$

In this model, α is known as the reaction extent or conversion and is determined by equation (5)

$$\alpha = \frac{m_0 - m_t}{m_0 - m_\infty} \tag{5}$$

Where $\mathbf{m_0}$, $\mathbf{m_t}$, and $\mathbf{m_\infty}$ are the initial mass, the mass in time **t**, and the mass at the end of the reaction.

Using the data obtained from the TGA analysis and applying the $g(\alpha)$ function, the apparent activation energy *Ea* and the pre-exponential factor are obtained with the slope and the intercept by performing the linear fit with values of $R^2 > 0.9$ resulting from graphing $g(\alpha)$ versus $1/T$.

The $g(\alpha)$ model used in this study refers to the reaction mechanism in which the interface gradually moves towards the core of the soot particles, so the volume of the soot decreases progressively while the reaction occurs on the surface due to the action of oxygen on it until finally the soot particle is wholly consumed.

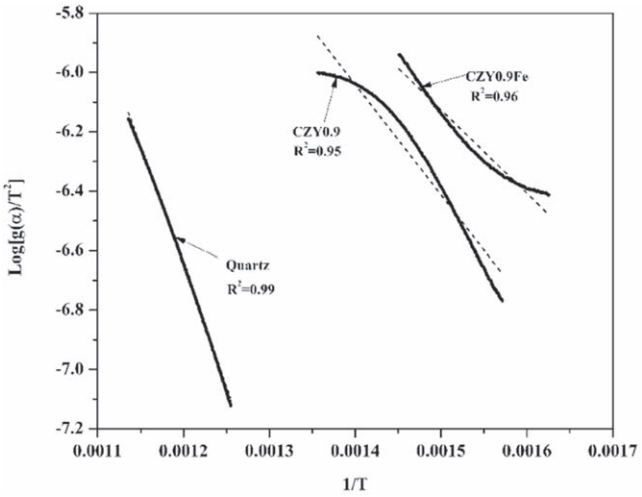

Figure 10. Estimated apparent activation energy values by using quartz, CZY0.9, and CZY0.9Fe as catalysts.

Table 5. Obtained kinetic parameters by the Coast-Redfern method.

Catalyst	Temperature range $0.15 \leqslant \alpha \leqslant 0.90$	Ea (KJ · mol^{-1})	A (min^{-1})	R^2
Quartz	523 to 607 °C	155	21.4×10^7	0.998
CZY0.9	363 to 465 °C	71.2	12.55×10^3	0.946
CZY0.9Fe	342 to 416 °C	53.9	8.2×10^2	0.961

Figure 9 shows the reaction's extent based on temperature, where CZY0.9Fe oxide is observed to have a higher conversion rate than CZY0.9 oxides, indicating the synergistic effects of Fe_2O_3 on the catalyst behavior.

Figure 10 shows the curves obtained from graphing $g(\alpha)$ versus $1/T$ using TGA analysis data. It is displayed the fitting curve with values of $R^2 > 0.9$. The activation energy and the pre-exponential factor value A were calculated from the slope and the intercept.

Table 5 shows the kinetic parameters obtained based on the linear regression of the ATG study's data. The temperature range considered for the determination of kinetic parameters was defined between T_{15} and T_{90}; therefore, the reaction progress was calculated in the same range. The lower activation energy was observed in the CZY0.9Fe catalyst. Results indicate that the Fe_2O_3 phase promotes a reduction for the energy requirements for the soot oxidation reaction to occurs.

4. Conclusions

A series of ternary oxides of general formula $Ce_{1-x}(Zr + Y)_xO_{2-\delta}$ was successfully synthesized by following the citrate-EDTA precursor approach. The oxides showed excellent thermal stability and high specific surface area values even after heat treatment at 600 °C. Furthermore, Fe_2O_3 nanoparticle deposits were made using the thermal decomposition of metalorganic precursors route. The characterization corroborated the presence of the Zr and Y doping elements and the deposit of Fe_2O_3 particles that were highly dispersed in the materials. Additionally, Ramman spectroscopy analyses revealed the formation of extrinsic oxygen vacancy in ternary oxides and confirmed the presence of Fe_2O_3. Soot oxidation studies conducted by TGA showed that CZY0.7Fe and CZY0.9Fe ternary oxides exhibit excellent catalytic behavior for soot oxidation compared to CeO_2 by drastically decrease the T10, T_{50}, and T_{90} temperatures to 310 °C, 383 °C, and 416 °C, respectively. The kinetic parameters determined for the soot oxidation reaction with the CZY0.9Fe catalyst show that the Fe_2O_3 phase promotes the oxidation reaction with a lower energy requirement.

Acknowledgments

This work was supported by Proyectos de Investigación Científica y Desarrollo Tecnológico SIP-IPN No. 20202003. The authors, wish to express their appreciation for the SIBE-IPN, EDI-IPN and BEIFI-IPN programs. Part of the scientific and technological infrastructure used here, was acquired thanks to the program Infraestructura CONACyT-2019 Project No. 301908.

ORCID iDs

J Ortiz-Landeros https://orcid.org/0000-0002-8319-7448

References

[1] Gu Z, Sang X, Wang H and Li K 2014 Structure and catalytic property of CeO_2–ZrO_2–Fe_2O_3 mixed oxide catalysts for diesel soot combustion: effect of preparation method *J. Rare Earths* **32** 817–23
[2] Mohankumar S and Senthilkumar P 2017 Particulate matter formation and its control methodologies for diesel engine: a comprehensive review *Renew. Sustain. Energy Rev.* **80** 1227–38
[3] Bayat R, Ashra K, Sha M and Hassanvand M S 2019 Health impact and related cost of ambient air pollution in Tehran *Environ. Res.* **176** 108547
[4] Mishra R K 2017 Air pollution health risk based on AirQ + Software tool *Int. J. Appl. Reseach Technol.* **2** 190–199 Air pollution health risk based on AirQ+Software tool
[5] Das D D *et al* 2017 Sooting tendencies of diesel fuels, jet fuels, and their surrogates in diffusion flames *Fuel* **197** 445–58
[6] Apte J S, Marshall J D, Cohen A J and Brauer M 2015 Addressing global mortality from ambient PM2.5 *Environ. Sci. Technol.* **49** 8057–66
[7] Brook R D *et al* 2015 Particulate matter air pollution and cardiovascular disease an update to the scientific statement from the american *AHA Sci. Statement.* **121** 2331–2378
[8] Meyer A, Czerwinsky J, Matter U, Wyser M, Scheidegger W and Kieser D 1998 Diesel nano-particulate emissions: properties and reduction strategies *Eng. Soc. Adv. Mobil. L. Sea Air Sp.* **980539** 1–2
[9] Serrano J R, Arnau F J, Piqueras P and García-Afonso Ó 2013 Packed bed of spherical particles approach for pressure drop prediction in wall-flow DPFs (diesel particulate filters) under soot loading conditions *Energy* **58** 644–54
[10] Konstandopoulos A G 2000 Fundamental studies of diesel particulate filters: transient loading, regeneration and aging *SAE Technical Pap.* **01-1016** 1–23
[11] Andreata M, Millo F, Mallamo F, Torino P, Mercuri D and Pozzi C 2013 Experimental investigation on three different ceramic substrate materials for a diesel particulate filter *SAE Technical Pap.* **24-1** 1–11
[12] Orihuela M P, Gómez-Martín A, Miceli P, Becerra J A, Chacartegui R and Fino D 2018 Experimental measurement of the filtration efficiency and pressure drop of wall-flow Diesel Particulate Filters (DPF) made of biomorphic Silicon Carbide using laboratory generated particles *Appl. Therm. Eng.* **131** 41–53
[13] Becerra A, Chacartegui R, Orihuela M P and Aurora G 2017 Performance of biomorphic Silicon Carbide as particulate filter in diesel boilers *J. Environ. Manage.* **203** 907–19
[14] Warner J R, Dobson D, Cavataio G and Co F M 2010 A study of active and passive regeneration using laboratory generated soot on a variety of SiC diesel particulate filter formulations *SAE Int.* **3** 149–164
[15] Wu X 2014 Roles of acid sites on Pt/H-ZSM5 catalyst in catalytic oxidation of diesel soot *ACS Catal.* **5** 909–919
[16] Kim C H, Schmid M, Schmieg S J, Tan J and Li W 2011 The effect of Pt-Pd ratio on oxidation catalysts under simulated diesel exhaust *SAE Int.* **2011-01** 1134-1144
[17] Liu J, Zhao Z, Xu C and Duan A 2008 Simultaneous removal of NO_x and diesel soot over nanometer Ln–Na–Cu–O perovskite-like complex oxide catalysts *Appl. Catal.* **78** 61–72
[18] Xu J *et al* 2010 Three-dimensionally ordered macroporous $LaCo_xFe_{1-x}O_3$ perovskite-type complex oxide catalysts for diesel soot combustion *Catal. Today* **153** 136–42
[19] Wang X, Zhang Y, Li Q, Wang Z and Zhang Z 2012 Identification of active oxygen species for soot combustion on $LaMnO_3$ perovskite *Catalysis Science & Technology* **2** 1822
[20] Zhang M, Jin B, Liu Y, Liu W, Weng D and Wu X 2019 Ozone activated Ag/CeO_2 catalysts for soot combustion: the surface and structural influences *Chem. Eng. J.* **375** 121961
[21] Dhakad M, Mitshuhashi T, Rayalu S, Doggali P and Bakardjiva S 2008 Co_3O_4–CeO_2 mixed oxide-based catalytic materials for diesel soot oxidation *Catal. Today* **132** 188–93
[22] Online V A *et al* 2017 Highly active MnO_x–CeO_2 catalyst for diesel soot combustion *RSC Adv.* **7** 3233–9
[23] Shan W, Ma N and Yang J 2010 Catalytic oxidation of soot particulates over MnO_x–CeO_2 oxides prepared by complexation-combustion method *J. Nat. Gas Chem.* **19** 86–90
[24] Li H, Li K, Wang H, Zhu X, Wei Y, Yan D, Cheng X and Zhai K 2016 Soot combustion over $Ce_{1-x}Fe_xO_2$ and CeO_2/Fe_2O_3 catalysts: roles of solid solution and interfacial interactions in the mixed oxides *Appl. Surf. Sci.* **390** 513–25
[25] Ma S, Che S, Zhao Z, Soomro A, Zhu M, Hu J, Wu M and Xiang W 2018 Enhanced hydrogen generation for Fe_2O_3/CeO_2 oxygen carrier via rare-earth (Y, Sm, and La) doping in chemical looping process *Energ. Fuel.* **32** 11362–74
[26] Li B, Raj A, Croiset E and Wen J Z 2019 Reactive Fe–O–Ce sites in ceria catalysts for soot oxidation *Catalysts* **9** 815
[27] Wagloehner S and Kureti S 2012 Study on the mechanism of the oxidation of soot on Fe_2O_3 catalyst *Appl. Catal. B: Environ.* **125** 158–65
[28] Andana T, Piumetti M, Bensaid S, Russo N, Fino D and Pirone R 2016 CO and soot oxidation over Ce–Zr–Pr oxide catalysts *Nanoscale Res. Lett.* **11** 1–9
[29] Yin A M K, Davis R J, Mahamulkar S, Jones C W, Agrawal P and Shibata H 2017 Catalytic oxidation of solid carbon and carbon monoxide over cerium-zirconium mixed oxides *AlChE* **63** 725–38
[30] Ovalle-Encinia O, Pfeiffer H, Fabián-Anguiano J A and Ortiz-Landeros J 2019 Nanosized lithium aluminate (γ-$LiAlO_2$) synthesized by EDTA-citrate complexing method, using different thermal conditions *J. Mex. Chem. Soc.* **63** 229–45
[31] Fuentes R O and Baker R T 2009 Synthesis of nanocrystalline CeO_2–ZrO_2 solid solutions by a citrate complexation route: a thermochemical and structural study *J. Phys. Chem.* C **113** 914–24
[32] Vargas-García J R, Mercado-Zuñiga C, Torres-Torres C, Trejo-Valdez M, Torres-Martinez R and Cervantes-Sodi F 2014 Influence of silver decoration on the nonlinear optical absorption exhibited by multiwall carbon nanotubes *J. Nanopart. Res.* **16** 2334-2342
[33] Doebelin N and Kleeberg R 2015 Profex : a graphical user interface for the Rietveld refinement program BGMN *J. Appl. Crystallogr.* **48** 1573–80
[34] Klug H and Alexander L 1974 *X-ray Diffraction Procedures: For Polycrystaline and Amorphous Materials.* 2nd edn (New York: Wiley) 978-0-471-49369-3
[35] Li L *et al* 2011 Study of defect sites in $Ce_{1-x}MxO_{2-\delta}$ (x = 0.2) solid solutions using raman spectroscopy *J. Phys. Chemistry* A **115** 7972–7

[36] Lowell M T S, Shields J E and Thomas M A 2004 *Characterization of Porous Solid and Powders: Surface Area, Pore size and Density* (*Particle Technology Series*) (Netherlands: Springer) 1-4020-2302-2
[37] Cychosz M T K A, Guillet-Nicolas R and García-Martínez J 2016 Recent advances in the textural characterization of hierarchically structured nanoporous materials *Chem. Soc. Rev.* **46** 389–414
[38] Patil S, Seal S, Guo Y, Schulte A and Norwood J 2006 Role of trivalent La and Nd dopants in lattice distortion and oxygen vacancy generation in cerium oxide nanoparticles *Appl. Physic Lett.* **88** 243110
[39] Vinodkumar T, Rao B G and Reddy B M 2015 Influence of isovalent and aliovalent dopants on the reactivity of cerium oxide for catalytic applications *Catal. Today* **253** 57–64
[40] Mansour H, Letifi H, Bargougui R, De Almeida-Didry S, Negulescu B, Autret-Lambert C, Gadri A and Ammar S 2017 Structural, optical, magnetic and electrical properties of hematite (α-Fe_2O_3) nanoparticles synthesized by two methods: polyol and precipitation *Appl. Phys.* A **123** 787
[41] Jubb A M and Allen H C 2010 Vibrational spectroscopic characterization of hematite, maghemite, and magnetite thin films produced by vapor deposition *Appl. Mater. Interfaces* **2** 2804–12
[42] Schilling C, Hofmann A, Hess C and Ganduglia-Pirovano M V 2017 *J. Phys. Chem.* C **121** 20834–49
[43] Liu S *et al* 2016 Soot oxidation over CeO_2 and Ag/CeO_2: factors determining the catalyst activity and stability during reaction *J. Catal.* **337** 188–98
[44] Nascimento L F, De Sousa Filho P C, Lima J F and Serra O A 2015 Kinetic parameters of soot oxidation catalyzed by nanosized ZnO–CeO_2 solids *J. Braz. Chem. Soc.* **26** (7) 1315–1320
[45] Ebrahimi-Kahrizsangi R and Abbasi M H 2008 Evaluation of reliability of Coats-Redfern method for kinetic analysis of non-isothermal TGA *Trans. Nonferrous Met. Soc. China* **18** 217–21